Indones. J. Chem., 2022, 22 (2), 539 - 547

539

Microstructural Analysis and Antibacterial Response of Zn²⁺/Mg²⁺ Dual Doped β-Tricalcium Phosphate Bioceramics

Ammar Zeidan Alshemary[1,2*], Huda Basim Qasim[3], and Ali Taha Saleh[4]

[1]*Department of Biomedical Engineering, Faculty of Engineering, Karabuk University, Karabuk 78050, Turkey*

[2]*Biomedical Engineering Department, Al-Mustaqbal University College, Hillah, Babil 51001, Iraq*

[3]*Al-Manara College for Medical Sciences, Misan 62001, Iraq*

[4]*Department of Chemistry, College of Science, University of Misan, Misan 62001, Iraq*

Abstract: *This article evaluates the impact of the addition of zinc (Zn) and magnesium (Mg) on the structural, morphological, and antibacterial characteristics of β-tricalcium phosphates (hereafter called Zn/Mg-βTCP) prepared using the microwave (MW) assisted wet precipitation method in which the Ca deficient apatite $[Ca_{9-(x+y)}Mg_xZn_y(HPO_4)(PO_4)_5(OH)]$ was calcined for 2 h at 1000 °C. The prepared samples were characterized using XRD, FTIR, and FESEM measurements. The XRD patterns of the samples showed a steady decrease in the lattice parameters with an increase in Mg^{2+} and Zn^{2+} content. The FESEM images of the samples disclosed the morphological changes due to the Mg^{2+}/Zn^{2+} co-doping. The inclusion of Mg^{2+} and Zn^{2+} into the βTCP was shown to induce excellent bioactivities that were absent in the pristine βTCP. Enhancement, coupled with good antimicrobial properties against Escherichia coli (E. coli), suggests that Mg^{2+}/Zn^{2+} co-doping TCP can be developed further into antibacterial bone cement. As synthesized, it would be considered a potential biomaterial for orthopedic applications.*

Keywords: *β-tricalcium phosphates; Co-doping; microstructure; phase purity; antibacterial*

■ INTRODUCTION

Microbes infecting the bone create osteomyelitis, an inflammation of the bone that may be fatal. Osteomyelitis is often treated with basic surgical debridement of diseased bones, appropriate soft tissue covering, and antibiotics. Long-term antibiotic medication is necessary, usually lasting 4–6 weeks but sometimes much longer [1]. Oral antibiotics may cause systemic toxicity, including renal and hepatic problems, and have low penetration into the targeted region [2-4]. It is thus necessary to investigate other methods of administering antibiotics. The unique bioactivities, biocompatibilities, and osteoconductive traits of the calcium phosphates (CPs) based materials make them ideal for a wide range of biomedical uses. They are very effective for implant-bone tissues in dental and orthopedic reconstructive medicines [5-8]. Presently, Hydroxyapatite (HA) and β-tricalcium phosphates (βTCP) are extensively used for bone tissue grafting due to their non-stimulating nature of bone generation and resorption inhibition [9-10]. βTCP and HA-based materials doped with trace elements such as Zinc (Zn) and Magnesium (Mg) have been shown to stimulate exceptional bioactivities that are missing in their parent counterparts [11-12].

In recent years, the inclusion of different dopants (Mg^{2+}, Sr^{2+}, and Zn^{2+}) ions into the structure of the CPs received focused attention due to their significant role in diverse biological processes [13]. Zn is one of the most vital trace elements responsible for various cellular processes in the human body, such as DNA replication, behavioral responses, reproductions, virilities, bone generation, bone growth, and wound healing. Furthermore, Zn is essential in genetic expression, cellular growth regulation, and cell differentiation [14].

A recent study revealed a clinical correlation between osteoporosis and a deficiency of Zn in the human body [15]. The main reason for the biocompatibility of Zn is due to its matching ionic radius (0.075 nm) with the bone tissue element. Meanwhile, the bone tissues' slow resorption of the βTCP ceramics makes them highly biocompatible [16]. Chen et al. synthesized nanorods of Zn doped HA and found that the presence of Zn inhibited the growth of *Aggregatibacter actinomycetemcomitans*, *Fusobacterium nucleatum*, and *Streptococcus mutant* bacteria [17]. Bhattacharjee et al. demonstrated that incorporation of Zn improved the antibacterial efficacy of HA against *Escherichia coli* and *Staphylococcus aureus* bacteria [18].

The element of Mg participates in diverse biological activities of humans, such as cellular proliferation and differentiation, cell-matrix interactions, and the usual functions of the organs [19]. The significance of Mg concerning the human bone structures is well-known, especially the prevention of the potential risks related to osteoporosis [20]. On top of that, Mg is crucial for the calcification processes, bone fragility, and minerals' metabolic activities [21]. Synthetic materials containing metal ions can be destructive if the ions are highly concentrated and are poisonous to human cells in high concentrations [8]. Materials containing metal ions such as Zn^{2+}, Ag^+, and Cu^{2+} can be used to combat post-operative infections, as these ions exhibit antimicrobial activity and are non-cytotoxic at low concentrations. Because of the significance of the indispensable elements Zn and Mg in the human body's functioning, some Zn/Mg co-doped βTCP were synthesized via the microwave (MW) assisted wet precipitation technique and characterized using different analytical tools. The structures and morphologies of the as-prepared samples were evaluated as a function of varying Zn/Mg contents to determine the feasibility of improving bioactivities. The antibacterial efficiency results were analyzed, interpreted, and discussed.

■ EXPERIMENTAL SECTION

Materials

The Zn/Mg-TCP was prepared using analytical grade high purity chemical reagents (Qrec, New Zealand) of calcium nitrate $[Ca(NO_3)_2\cdot4H_2O]$, diammonium hydrogen phosphate $[(NH_4)_2HPO_4]$, magnesium nitrate $[(Mg(NO_3)_2\cdot6H_2O)]$, zinc nitrate $[Zn(NO_3)_2]$, and ammonium hydroxide $[(NH_4OH)]$.

Instrumentation

The samples crystal structures and purity of the phases were examined using the X-ray diffractometer (Bruker D8 Advance XRD). The samples morphology was imaged via a field emission scanning electron microscope (FESEM, Zeiss-LEO 1530). The elemental compositional analyses of the samples were carried out using an energy dispersive X-ray spectrometer (EDX, Swift ED 3000 from the Oxford Instruments, operated at 20 kV). The chemical functional groups in the samples were detected using Fourier transform infrared spectroscopy (FTIR, Nicolet iS50 spectrometer) following the classic KBr pellet technique. The FTIR spectra (in the transmission mode) were recorded in the range of 400–4000 cm^{-1} with 32 scans at a resolution of 4 cm^{-1}. All the characterizations of the calcined samples (at 1000 °C) were performed at room temperature.

Procedure

The experimental steps, including the preparation of Zn/Mg-βTCP and antimicrobial test, as a flowchart, are presented in Fig. 1.

Preparation of Zn/Mg-βTCP materials

The pristine βTCP and Zn/Mg-βTCP were made via the MW-assisted wet precipitation technique where the Ca/P and (Ca+Mg+Zn)/P molar ratio was kept at 1.5. The $[Ca(NO_3)_2\cdot4H_2O]$ (4.250 g) was first dissolved in 100 mL of double-distilled water (DDW), then drops of $[(NH_4)_2HPO_4]$ were added, and the mixture was continuously stirred. The pH of the mixture was set at 7.4 via the addition of NH_4OH solution (8 M). Next, the resultant mixture was processed for 5 min in an MW oven (SHARP, model R-218LS, operated at 800 W) before being filtrated and rinsed using DDW. Then, the filtered specimen was dried for 17 h in an oven at 80 °C, then calcinated for 2 h at 1000 °C to achieve the βTCP. The Zn/Mg-TCP was prepared in the same manner, using the appropriate amounts of $[Mg(NO_3)_2\cdot6H_2O]$
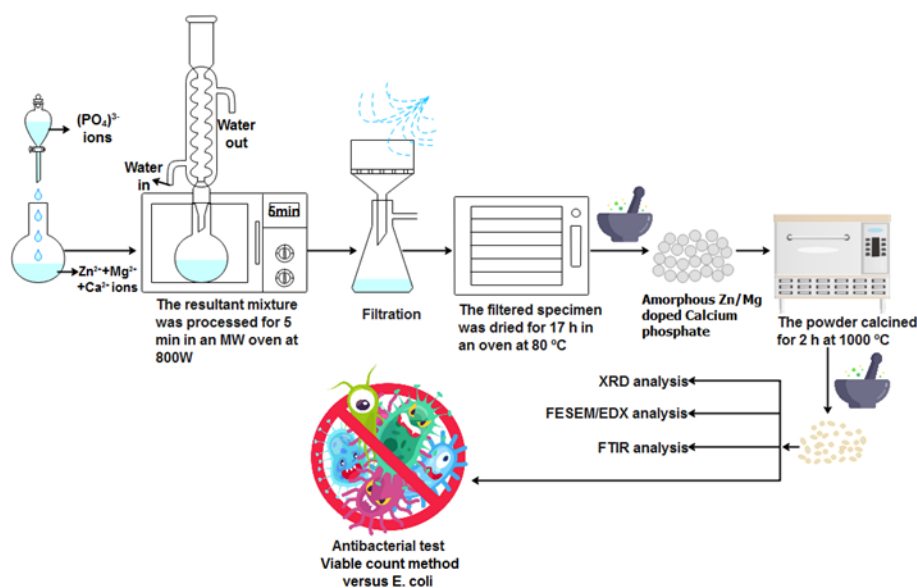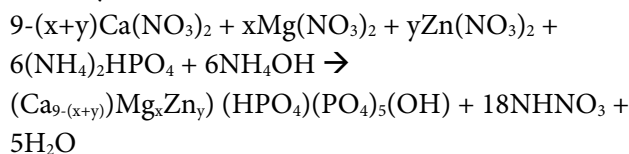
Fig 1. Experiment flow chart

(0.2, 0.3, 0.4, 0.5 M) (0.780, 1.170, 1.561, 1.951 g respectively), [$Zn(NO_3)_2$] (0.2, 0.3, 0.4, 0.5 M) (0.757, 1.136, 1.515 and 1.894 g respectively), and [$Ca(NO_3)_2 \cdot 4H_2O$] (8.6, 8.4, 8.2 and 7 M) (4.061, 3.967, 3.872 and 3.306 g respectively). Table 1 enlists the chemical compositions (in mol) of the produced samples with various concentrations of Zn and Mg with their respective codes. The production of the βTCP and Zn/Mg-βTCP can be described using the following chemical reaction pathways:
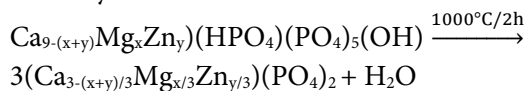
Pathway I:

$9-(x+y)Ca(NO_3)_2 + xMg(NO_3)_2 + yZn(NO_3)_2 +$
$6(NH_4)_2HPO_4 + 6NH_4OH \rightarrow$
$(Ca_{9-(x+y)})Mg_xZn_y)(HPO_4)(PO_4)_5(OH) + 18NHNO_3 + 5H_2O$

Pathway II:

$Ca_{9-(x+y)}Mg_xZn_y(HPO_4)(PO_4)_5(OH) \xrightarrow{1000°C/2h}$
$3(Ca_{3-(x+y)/3}Mg_{x/3}Zn_{y/3})(PO_4)_2 + H_2O$

Table 1. Chemical compositions (in mol) of the obtained samples with their codes

Sample code	Ca^{2+}	PO_4^{3-}	Mg^{2+}	Zn^{2+}	Mg+Zn
βTCP	9	6	0.0	0.0	0.0
(0.4)Zn/Mg-βTCP	8.6	6	0.2	0.2	0.4
(0.6)Zn/Mg-βTCP	8.4	6	0.3	0.3	0.6
(0.8)Zn/Mg-βTCP	8.2	6	0.4	0.4	0.8
(1.0)Zn/Mg-βTCP	7.0	6	0.5	0.5	1.0

Antimicrobial tests

The antibacterial efficiency of pure and Zn/Mg doped

βTCP materials were evaluated quantitatively through the viable count method versus *Escherichia coli* (*E. coli*, ATCC 25922 strains). A standard mixture of 1 mL *E. coli* and 9 mL Luria-Bertani (LB) broth was incubated at 37 °C for a day, shaking at 250 rpm. The materials were sterilized and blended with the standard solution. The sterilized mixture (0.10 mL) was immunized on LB agar plates, then brooded at 37 °C. Lastly, the number of colonies developing units was tallied.

■   **RESULTS AND DISCUSSION**

Fig. 2 displays the XRD patterns of the produced samples, which consisted of several crystalline peaks at 25.82°, 27.77°, 29.64°, 31.02°, 32.4756°, and 34.38° corresponding to the growth along the (1 0 1 0), (2 1 4), (3 0 0), (0 2 1 0), (1 2 8), and (2 2 0) lattice plane orientations. The observed indexed peaks were matched with JCPDS card number of 09-0169 for the crystalline βTCP. Table 2 shows the lattice parameters, cell volume, and degree of crystallinity of the studied samples obtained from the XRD data analyses. The lattice plane directions for the pristine βTCP verified the growth of
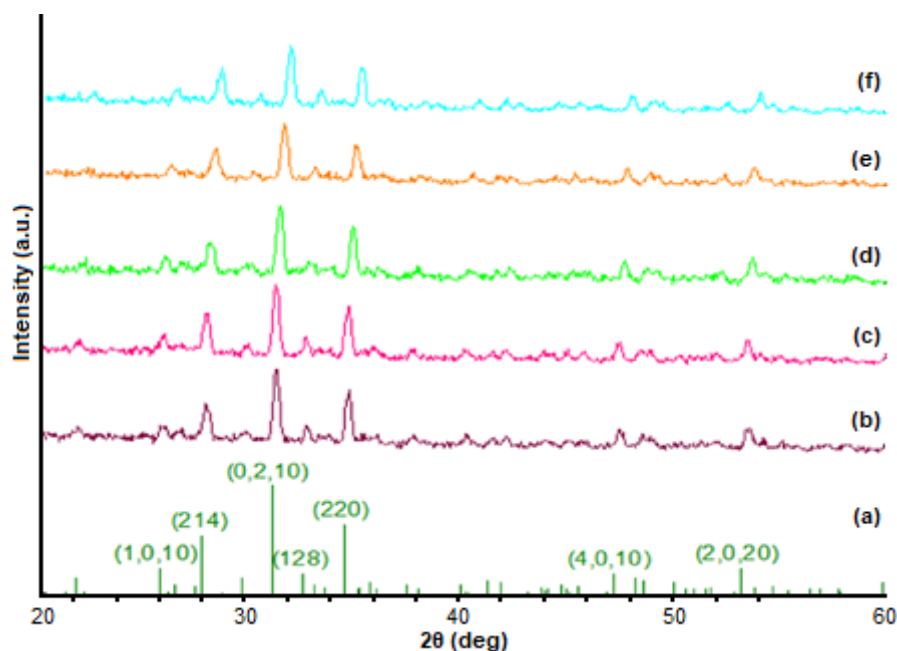
Fig 2. XRD patterns of the βTCP (JCPDS 09-0169) (a), βTCP (b), (0.4)Zn/Mg-βTCP (c), (0.6)Zn/Mg-βTCP (d), (0.8)Zn/Mg-βTCP (e), and (1.0)Zn/Mg-βTCP (f)

Table 2. Lattice parameters, cell volume, and degree of crystallinity of the studied samples

Samples code	Chemical formula	Lattice parameters			DC*
		a(Å)	c(Å)	V(Å)³**	
βTCP (JCPDS 09-0169)	$Ca_3(PO_4)_2$	10.429	37.380	3520.9	---
βTCP	$Ca_9(PO_4)_6$	10.460	37.391	3532.6	88
(0.4)Zn/Mg-βTCP	$Ca_{8.6}Mg_{0.2}Zn_{0.2}(PO_4)_6$	10.445	37.360	3529.7	81
(0.6)Zn/Mg-βTCP	$Ca_{8.4}Mg_{0.3}Zn_{0.3}(PO_4)_6$	10.421	37.354	3524.0	77
(0.8)Zn/Mg-βTCP	$Ca_{8.2}Mg_{0.4}Zn_{0.4}(PO_4)_6$	10.415	37.254	3521.5	69
(1.0)Zn/Mg-βTCP	$Ca_{7.0}Mg_{0.5}Zn_{0.5}(PO_4)_6$	10.410	37.222	3514.2	64

*Degree of crystallinity, **Cell volume

the hexagonal crystals with the lattice constants of a = b = 10.4592 Å and c = 37.3914 Å as depicted in Table 2. The inclusion of Mg^{2+}/Zn^{2+} into the βTCP lattice structures diminished the intensity of the Bragg's peaks accompanied by a shift toward higher diffraction angles (values of 2θ), as indicated in Fig. 2. The observed reduction in the sample's degree of crystallinities (from 88 to 64) was due to the replacement of the Ca^{2+} ions, which have larger ionic radii (0.99 Å) by the Mg^{2+} (0.65 Å) ions and Zn^{2+} (0.74 Å) which they have smaller ionic radii.

Furthermore, the XRD pattern did not reveal any other crystalline phases, confirming the purity of the sample [13]. The intense XRD peak calculated the mean crystallite diameter following the Debye–Scherrer

formula. The mean size of the βTCP and Zn/Mg-βTCP was 36 nm and 28 nm, respectively. The lattice values of a and c were gradually decreased with a rise in Mg^{2+} and Zn^{2+} contents (Table 2). These shortening in the lattice constants were mainly due to the substitution of the Ca^{2+} by Mg^{2+}/Zn^{2+}, where the disparity in their ionic radii played a significant role. The values of a and c were reduced from 10.4452–10.4101 Å and 37.2217–37.3598 Å, respectively, with the addition of Mg^{2+}/Zn^{2+} into the βTCP structures. Meanwhile, cell volumes of the samples were reduced from 3529.7 to 3514.2 with the increase in Mg^{2+}/Zn^{2+} doping levels into the βTCP structures.

Fig. 3 illustrates the FTIR spectra of all the prepared samples, which consisted of several

characteristic vibration bands of the phosphate groups and water molecules. The pristine βTCP revealed a broad vibration band at around 3440 cm^{-1} due to the OH$^-$ from adsorbed water. The bands at approximately 1020 and 558 cm^{-1} were due to the vibration of the PO$_4^{3-}$ units. The bands at around 618 and 548 cm^{-1} were related to the bending vibrations (v_4) of the O–P–O linkages. The bands due to the stretching vibrations (v_3 and v_1) of the P–O bond occurred at approximately 955 cm^{-1}, 1033, and 1135 cm^{-1}. The bands appeared at around 1643 and 3448 cm^{-1} due to the adsorbed water's bond vibrations. The characteristics bands at 962 cm^{-1}, 1122 cm^{-1} to 939 cm^{-1}, and 1150 cm^{-1} corresponding to the phosphate vibrations were broadened and shifted as the doping contents of Mg^{2+}/Zn^{2+} were increased, implying the decrease in the crystallinity of the sample, which is consistent with the XRD results (Fig. 2). The nonexistence of the characteristic bands at 630 and 3570 cm^{-1} in the produced samples validated the complete absence of any HA as the secondary phase. The band assignments are summarized in Table 3.

Fig. 4 depicts the FESEM images of all the produced samples. The microstructures of the βTCP were comprised of dense (compact with nearly spherical crystallites without voids and cracks) aggregated particles with irregular morphology (Fig. 4(a)). Moreover, the morphologies of the Mg^{2+}/Zn^{2+} co-doped βTCP specimens were appreciably altered into interconnected structures (less compact and ginger-like pattern with many voids) with a clustering tendency (Fig. 4(b-e)). The

particle size of βTCP materials gradually decreased with the addition of Mg^{2+}/Zn^{2+} ions.

Table 4 compares the chemical composition of various products obtained from the EDX elemental analyses with the theoretical estimates. The close
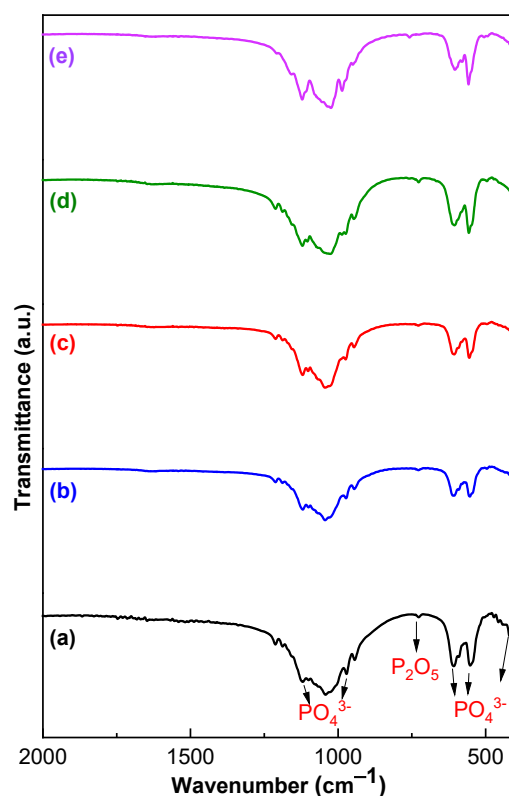

Fig 3. FTIR spectra of (a) βTCP, (b) (0.4) Zn/Mg-βTCP, (c) (0.6)Zn/Mg-βTCP, (d) (0.8)Zn/Mg-βTCP, and (e) (1.0)Zn/Mg-βTCP

Table 3. Band assignments for βTCP and Zn^{2+}/Mg^{2+} doped βTCP materials [22]

Peak number	Wavenumber (cm^{-1})	Band assignment
1	427	Stretching mode of PO$_4^{3-}$ group (v_2)
2	545–601	Bending mode of the PO$_4^{3-}$ group (v_4)
3	727–1212	Stretching modes of P–O–P and P=O in P$_2$O$_7$ group
4	941–971	Stretching mode of PO$_4^{3-}$ group (v_1)

Table 4. Chemical composition of various products obtained from the EDX analyses compared with the theoretical estimates

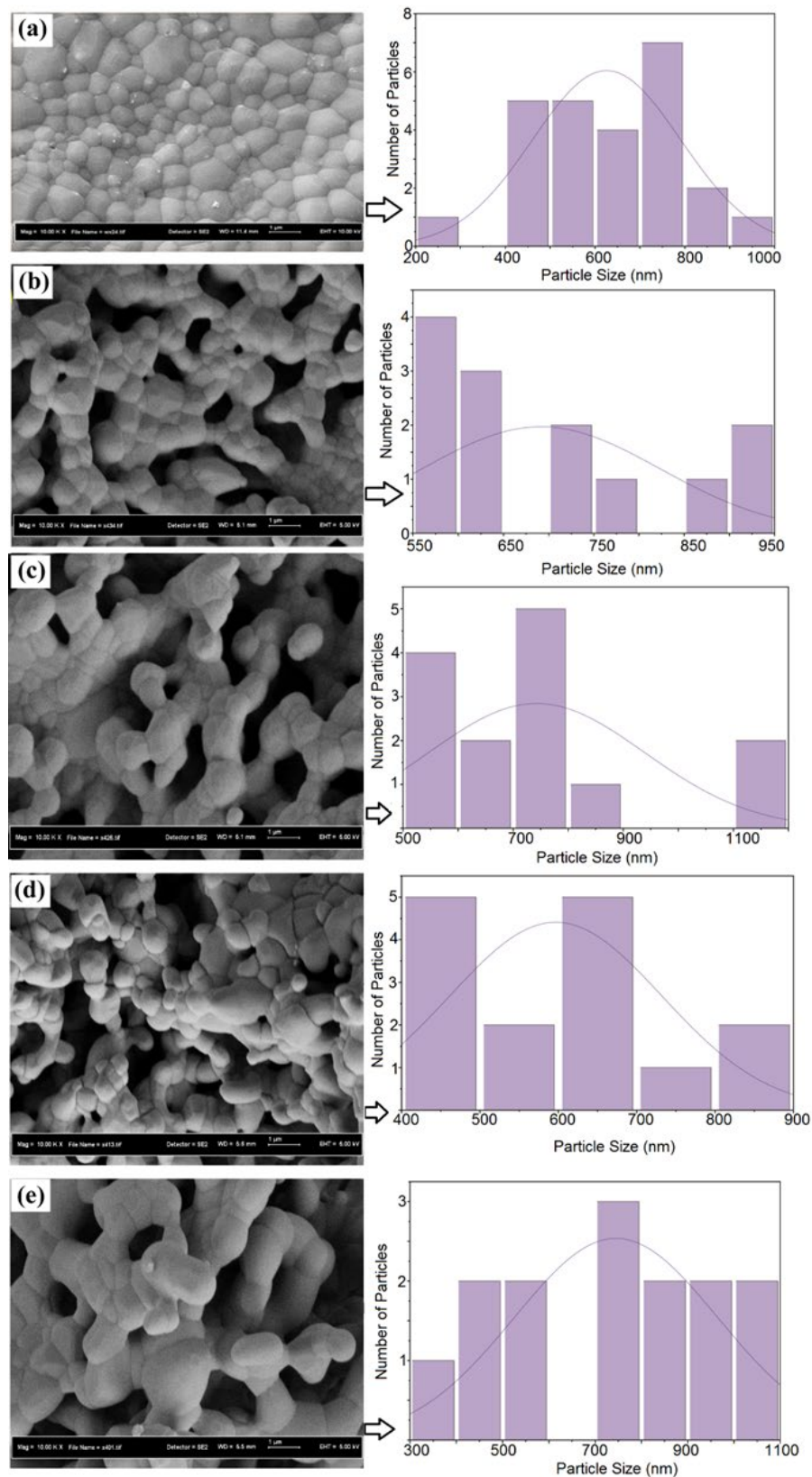| Samples code	Theoretical ratios Zn+Mg/Ca= X$_{MgZn}$	Measured ratios Zn+Mg/Ca= X$_{MgZn}$
βTCP	0.000	0.000
(0.4)Zn/Mg-βTCP	0.040	0.038
(0.6)Zn/Mg-βTCP	0.060	0.059
(0.8)Zn/Mg-βTCP	0.080	0.078
(1.0)Zn/Mg-βTCP	0.100	0.099

544

Indones. J. Chem., 2022, 22 (2), 539 - 547

Fig 4. FESEM images of (a) βTCP, (b) (0.4)Zn/Mg-βTCP, (c) (0.6)Zn/Mg-βTCP, (d) (0.8)Zn/Mg-βTCP, and (e) (1.0)Zn/Mg-βTCP. Particles size distribution attached with the SEM images
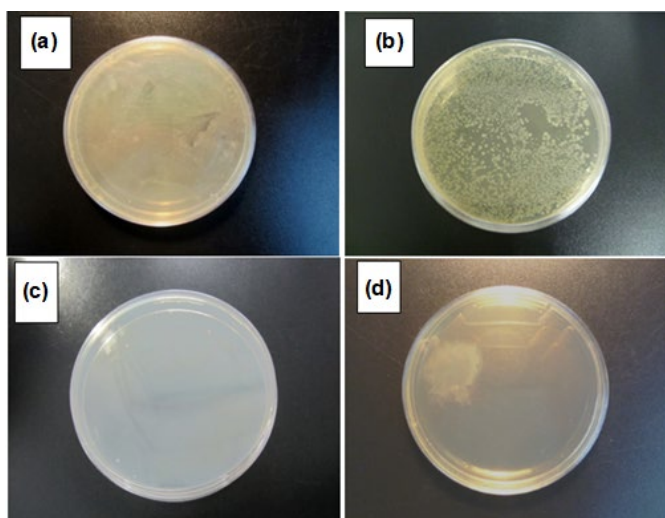
Fig 5. Descriptive photos of *E. coli* colonies on (a) (0.4)Zn/Mg-βTCP, (b) (0.6)Zn/Mg-βTCP, (c) (0.8)Zn/Mg-βTCP, and (d) (1.0)Zn/Mg-βTCP

agreement between the theoretical and experimental values of the trace elemental ratios confirmed the successful incorporation of the Mg^{2+}/Zn^{2+} into the βTCP crystal structure. In short, the inner consistency among the XRD, FTIR, and EDX results authenticated the adequate replacement of Ca^{2+} by the Mg^{2+}/Zn^{2+} dopants in the βTCP lattice sites.

The antibacterial activity of the Mg^{2+}/Zn^{2+} discharged from the Zn/Mg-βTCP was studied against the spread of *E. coli*. In this research, the viable count method assessed the antibacterial properties of Zn/Mg-βTCP materials. All samples were incubated with *E. coli* (ATCC 25922 strains) suspension for a day. Fig. 5 shows the substantial variance in bactericidal effect. The pure phase of βTCP materials has no ability to inhibit the growth of *E. coli* [23]. However, bacterial growth was inhibited by Zn/Mg-TCP nanocomposites. The number of *E. coli* colonies dwindled with an increase in the content of Mg^{2+}/Zn^{2+}. After a day of incubation in the plate containing (0.4) Zn/Mg-TCP and (0.6) Zn/Mg-TCP, hundreds of *E. coli* colonies were observed (Fig. 4(a, b)). However, a few bacterial colonies were observed in the agar plate containing (0.4) Zn/Mg-TCP. In contrast, no bacterial colonies were observed in the agar plates containing (0.8) Zn/Mg-βTCP and (1.0) Zn/Mg-βTCP (Fig. 4(c, d)).

CONCLUSION

Following the standard MW-assisted wet precipitation method, some Mg^{2+}/Zn^{2+} co-activated βTCP were produced. Thorough characterization was used to determine the Mg^{2+}/Zn^{2+} concentration-dependent structures and morphologies of dry and calcined (1000 °C) powdered specimens. The XRD analyses of the pristine and co-doped βTCP verified their hexagonal structure with phase purity where the lattice constants, cell volume, crystallinity, and crystallite size were found to decrease with the increase in the Mg^{2+}/Zn^{2+} concentrations. The FTIR spectral vibration bands revealed the existence of various characteristic functional groups related to βTCP and Zn/Mg-βTCP. The EDX analyses of the samples confirmed the appropriate elemental traces, thereby successfully incorporating the Mg^{2+}/Zn^{2+} dopants into the βTCP lattice. The FESEM surface morphologies of the sample manifested significant structural changes due to the substitution of Mg^{2+}/Zn^{2+} dopants, were more compact, void-free, and dense agglomerated irregular structures were gradually transformed into less compact and interconnected cluster-like networks with many voids. The results for the structures and morphologies were in good agreement. All these observations were ascribed to the replacement of the Ca^{2+} with larger ionic radii by the Mg^{2+}/Zn^{2+} having smaller ionic radii. The presented results suggest that the Mg^{2+}/Zn^{2+} containing βTCP cement is a very promising material for rapid antibacterial bone repair purposes. It is established that by selectively adjusting the Mg^{2+}/Zn^{2+} contents, the overall traits of the Zn/Mg-βTCP can be tailored, suggesting their suitability for diverse biomedical applications.

ACKNOWLEDGMENTS

REFERENCES

[1] Kumar, G.S., Govindan, R., and Girija, E., 2014, *In*

situ synthesis, characterization and *in vitro* studies of ciprofloxacin loaded hydroxyapatite nanoparticles for the treatment of osteomyelitis, *J. Mater. Chem. B*, 2 (31), 5052–5060.

[2] Shefy-Peleg, A., Foox, M., Cohen, B., and Zilberman, M., 2014, Novel antibiotic-eluting gelatin-alginate soft tissue adhesives for various wound closing applications, *Int. J. Polym. Mater. Polym. Biomater.*, 63 (14), 699–707.

[3] Mouriño, V., and Boccaccini, A.R., 2010, Bone tissue engineering therapeutics: controlled drug delivery in three-dimensional scaffolds, *J. R. Soc. Interface*, 7 (43), 209–227.

[4] Feng, W., Geng, Z., Li, Z., Cui, Z., Zhu, S., Liang, Y., Liu, Y., Wang, R., and and Yang, X., 2016, Controlled release behaviour and antibacterial effects of antibiotic-loaded titania nanotubes, *Mater. Sci. Eng., C*, 62, 105–112.

[5] Dai, J., Fu, Y., Chen, D., and Sun, Z., 2021, A novel and injectable strontium-containing hydroxyapatite bone cement for bone substitution: A systematic evaluation, *Mater. Sci. Eng., C*, 124, 112052.

[6] Han, B., Ma, P.W., Zhang, L.L., Yin, Y.J., Yao, K.D., Zhang, F.J., Zhang, Y.D., Li, X.L., and Nie, W., 2009, β-TCP/MCPM-based premixed calcium phosphate cements, *Acta Biomater.*, 5 (8), 3165–3177.

[7] Wang, S., Liu, R., Yao, J., Wang, Y., Li, H., Dao, R., Guan, J., and Tang, G., 2013, Fabrication of mesoporous magnesium substituted β-tricalcium phosphate nanospheres by self-transformation and assembly involving EDTA ions, *Microporous Mesoporous Mater.*, 179, 172–181.

[8] Prakash, C., Singh, S., Pabla, B.S., Sidhu, S.S., and Uddin, M.S., 2019, Bio-inspired low elastic biodegradable Mg-Zn-Mn-Si-HA alloy fabricated by spark plasma sintering, *Mater. Manuf. Processes*, 34 (4), 357–368.

[9] Horiuchi, S., Hiasa, M., Yasue, A., Sekine, K., Hamada, K., Asaoka, K., and Tanaka, E., 2014, Fabrications of zinc-releasing biocement combining zinc calcium phosphate to calcium phosphate cement, *J. Mech. Behav. Biomed. Mater.*, 29, 151–160.

[10] Kaygili, O., Keser, S., Bulut, N., and Ates, T., 2018, Characterization of Mg-containing hydroxyapatites synthesized by combustion method, *Physica B*, 537, 63–67.

[11] Calasans-Maia, M., Calasans-Maia, J., Santos, S., Mavropoulos, E., Farina, M., Lima, I., Lopes, R.T., Rossi, A., and Granjeiro, J.M., 2014, Short-term *in vivo* evaluation of zinc-containing calcium phosphate using a normalized procedure, *Mater. Sci. Eng., C*, 41, 309–319.

[12] Shahmohammadi, P., and Khazaei, B.A., 2021, Characterization of Zn/Mg-enriched calcium phosphate coating produced by the two-step pulsed electrodeposition method on titanium substrate, *Surf. Interfaces*, 22, 100819.

[13] Saleh, A.T., Ling, L.S., and Hussain, R., 2016, Injectable magnesium-doped brushite cement for controlled drug release application, *J. Mater. Sci.*, 51 (16), 7427–7439.

[14] Tas, A.C., Bhaduri, S.B., and Jalota, S., 2007, Preparation of Zn-doped β-tricalcium phosphate (β-Ca$_3$(PO$_4$)$_2$) bioceramics, *Mater. Sci. Eng., C*, 27 (3), 394–401.

[15] Mahdavi-Roshan, M., Ebrahimi, M., and Ebrahimi, A., 2015, Copper, magnesium, zinc and calcium status in osteopenic and osteoporotic post-menopausal women, *Clin. Cases Miner. Bone Metab.*, 12 (1), 18–21.

[16] Fadeeva, I.V., Gafurov, M.R., Kiiaeva, I.A., Orlinskii, S.B., Kuznetsova, L.M., Filippov, Y.Y., Fomin, A.S., Davydova, G.A., Selezneva, I.I., and Barinov, S.M., 2017, Tricalcium phosphate ceramics doped with silver, copper, zinc, and iron (III) ions in concentrations of less than 0.5 wt.% for bone tissue regeneration, *BioNanoScience*, 7 (2), 434–438.

[17] Chen, X., Tang, Q.L., Zhu, Y.J., Zhu, C.L., and Feng, X.P., 2012, Synthesis and antibacterial property of zinc loaded hydroxyapatite nanorods, *Mater. Lett.*, 89, 233–235.

[18] Bhattacharjee, A., Gupta, A., Verma, M., Murugan, P.A., Sengupta, P., Matheshwaran, S., Manna, I., and Balani, K., 2019, Site-specific antibacterial

efficacy and cyto/hemo-compatibility of zinc substituted hydroxyapatite, *Ceram. Int.*, 45 (9), 12225–12233.

[19] Hofmann, M.P., Mohammed, A.R., Perrie, Y., Gbureck, U., and Barralet, J.E., 2009, High-strength resorbable brushite bone cement with controlled drug-releasing capabilities, *Acta Biomater.*, 5 (1), 43–49.

[20] Frasnelli, M., Pedranz, A., Biesuz, M., Dirè, S., and Sglavo, V.M., 2019, Flash sintering of Mg-doped tricalcium phosphate (TCP) nanopowders, *J. Eur. Ceram. Soc.*, 39 (13), 3883–3892.

[21] Saleh, A.T., and Alameri, D., 2021, Microwave-assisted preparation of zinc-doped β-tricalcium phosphate for orthopedic applications, *Indones. J. Chem*, 21 (2), 376–382.

[22] Motameni, A., Dalgic, A.D., Alshemary, A.Z., Keskin, D., and Evis, Z., 2020, Structural and biological analysis of mesoporous lanthanum doped βTCP for potential use as bone graft material, *Mater. Today Commun.*, 23, 101151.

[23] Qin, L., Yi, J., Xuefei, L., Li, L., Kenan, X., and Lu, X., 2020, The preparation of a difunctional porous β-tricalcium phosphate scaffold with excellent compressive strength and antibacterial properties, *RSC Adv.*, 10, 28397–28407.